LANGMUIR

pubs.acs.org/Langmuir Article

Magnesium-Induced Strain and Immobilized Radical Generation on the Boron Oxide Surface Enhances the Oxidation Rate of Boron Particles: A DFTB-MD Study

Prithwish Biswas, C. Huy Pham, and Michael R. Zachariah*

Cite This: *Langmuir* 2023, 39, 13782−13789 Read Online

ACCESS | Metrics & More | Article Recommendations | Supporting Information

ABSTRACT: Despite their high gravimetric and volumetric energy densities, boron (B) particles suffer from poor oxidative energy release rates as the boron oxide (B_2O_3) shell impedes the diffusivity of O_2 to the particle interior. Recent experiemental studies have shown that the addition of metals with a lower free energy of oxidation, such as Mg, can reduce the oxide shell of B and enhance the energetic performance of B by ∼30−60%. However, the exact underlying mechanism behind the reactivity enhancement is unknown. Here, we performed DFTB-MD simulations to study the reaction of Mg vapor with a B_2O_3 surface. We found that the Mg becomes oxidized on the B_2O_3 surface, forming a MgB_xO_y phase, which induces a tensile strain in the B−O bond at the MgB_xO_y−B_2O_3 interface, simultaneously reducing the interfacial B and thereby developing dangling bonds. The interfacial bond straining creates an overall surface expansion, indicating the presence of a net tensile strain. The B with dangling bonds can act as active centers for gas-phase O_2 adsorption, thereby increasing the adsorption rate, and the overall tensile strain on the surface will increase the diffusion flux of adsorbed O through the surface to the particle core. As the overall B particle oxidation rate is dependent on both the O adsorption and diffusion rates, the enhancement in both of these rates increases the overall reactivity of B particles.

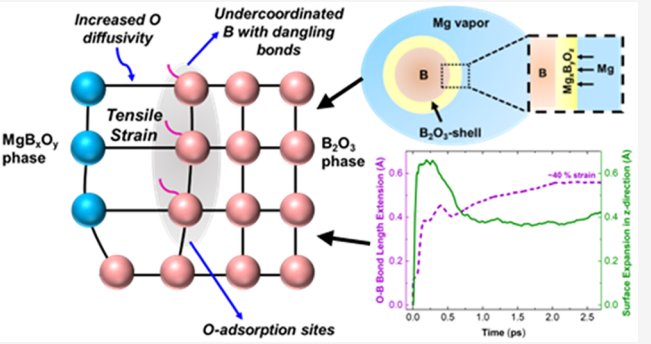

INTRODUCTION

With the highest oxidative energy density on both gravimetric and volumetric basis, boron (B) is extremely attractive as a fuel component in propulsion systems requiring maximal energy release rates.[1−5] In practice, however, achieving high energy release rates from B is often impeded by the unfavorable properties of the oxide shell on B particles.[6−9] B particles oxidize in a shrinking-core manner. When external or oxidative heating is applied, the boron oxide (B_2O_3) shell melts into a nonvolatile liquid at a relatively low temperature (∼720 K) compared to that of the B core, which remains solid during combustion.[10−13] The liquid shell devoid of any physical voids impedes the diffusivity of oxygen and hence the B oxidation process.[1−4,6,10,14] By contrast, metals with low melting or boiling points such as Al[15−18] and Mg[19−21] provide higher energetic performance, although having an inferior energy density compared to that of B, as they burn in the vapor phase.[15,17,22−24]

One of the strategies to overcome the liquid-phase mass transfer limitation is to use solid-state borohydrides such as ammonia borane that can generate gas-phase boron and hydrogen containing moieties.[25,26] Another approach to circumvent this limitation is to use an additive that will react with the oxide of boron. From a thermochemical perspective, the free energies of oxidation of metals such as Mg and Al are much lower than that of B,[27] which implies that metals such as Mg and Al can reduce B_2O_3 to elemental B. However, in the solid state the complete reduction of B_2O_3 will be inhibited by slow diffusion processes, and hence it is likely that Mg and Al will form mixed oxide phases with B on reacting with B_2O_3.[28] Recent studies on the energetic performance of Al/B and Mg/B composites prepared through ball-milling, plasma deposition, or physical mixing have reported an ∼30−60% enhancement (Figure 1(a)) in the reactivity of B on addition of Al and Mg as minor components.[28−34] The percent enhancement presented in Figure 1(a) is obtained from calorimetry, pressurization rate, burn time, or ignition delay measurements. In one of these studies, the highest enhancement in reactivity, ∼60%, has been reported for a 10 wt % Mg/B physically mixed nanoparticulate system.[34] A conjecture has been made that the Mg vapor (Figure 1(b)) generated from the Mg nanoparticle on heating

Received: April 13, 2023
Revised: August 27, 2023
Published: September 22, 2023

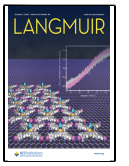

https://doi.org/10.1021/acs.langmuir.3c00982
Langmuir 2023, 39, 13782−13789

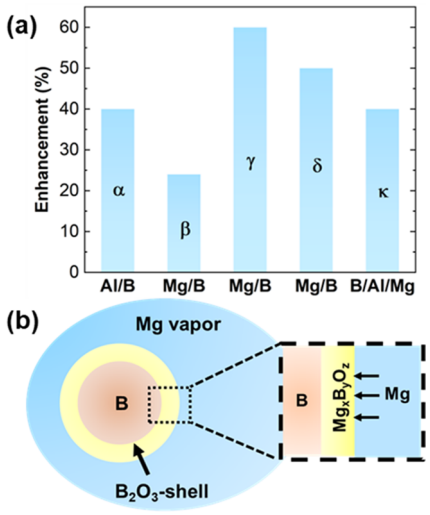

Figure 1. (a) Enhancement of the energy release rate of B with Al and Mg addition as reported by previous experimental studies (α,[29] β,[33] γ,[34] δ,[28] and κ[31]). (b) Schematic of how Mg vapor might manipulate the oxide shell of B, making the Mg/B composite the best-performing system.

reacts with the B_2O_3 shell to form a mixed Mg−B−O oxide phase having different physical properties than B_2O_3, which somehow enhances the rate of oxidation of B. However, experimentally probing the actual composition of the mixed oxide phase along with the exact atomic-scale mechanism behind the reactivity enhancement of B is nearly impossible. Hence, atomistic simulations are essential to addressing these questions.

In this study, we have investigated the reaction of vapor-phase Mg atoms with a B_2O_3 surface, through density functional theory tight binding[35−37]-molecular dynamics simulations (DFTB-MD) employing three-body interatomic interactions based on the Chebyshev Interaction Model for Efficient Simulation (CHIMES) framework.[38,39] DFTB being a semiempirical model is already less computationally expensive than DFT.[35] The CHIMES framework where the repulsive part of the DFTB energy functional is fitted to training data by a linear combination of Chebyshev polynomials further increases the computational efficiency of simulations of reactive systems having three-body interactions.[38]

Based on our simulation results, we show that Mg binds with the O atoms on the B_2O_3 surface to form MgB_xO_y phases. This results in tensile straining of the O−B bond at the developing MgB_xO_y−B_2O_3 interface. The excess volume created by the bond length extension is accommodated by an overall surface expansion. The interfacial boron is reduced and exists in an undercoordinated state, thereby developing dangling bonds, as a result of which it is available to particpate in subsequent reaction with external oxygen. The net tensile strain on the surface enhances the diffusion flux of adsorbed oxygen through the B_2O_3 shell. As the rate of oxidation of the B particles depends on the sum of the rate of adsorption of the O_2 to its surface and the rate of adsorbed O-ion diffusion through its shell, the simultaneous enhancement of both of these factors should enhance the overall oxidation rate of boron.

COMPUTATIONAL DETAILS

Semiempirical DFTB with self-consistent charge calculations has been described elsewhere.[38,39] The tight binding model assumes that electron densities are localized around the atom

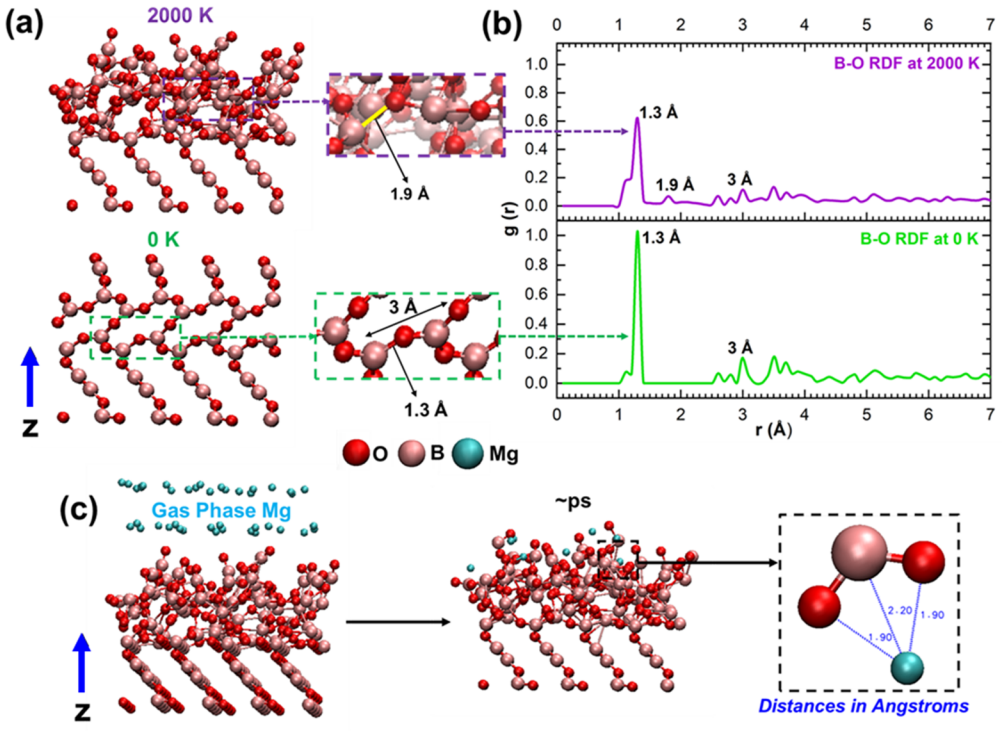

Figure 2. (a) Visual representation of the B_2O_3 (001) surface and B−O bond lengths, optimized at 0 K and after equilibration at 2000 K with the (b) corresponding radial distribution functions. (c) Visual representation of gas-phase Mg above the surface equilibrated at 2000 K and the surface post-Mg adsorption and representative illustration of the Mg−O and Mg−B bond lengths.

https://doi.org/10.1021/acs.langmuir.3c00982
Langmuir 2023, 39, 13782−13789

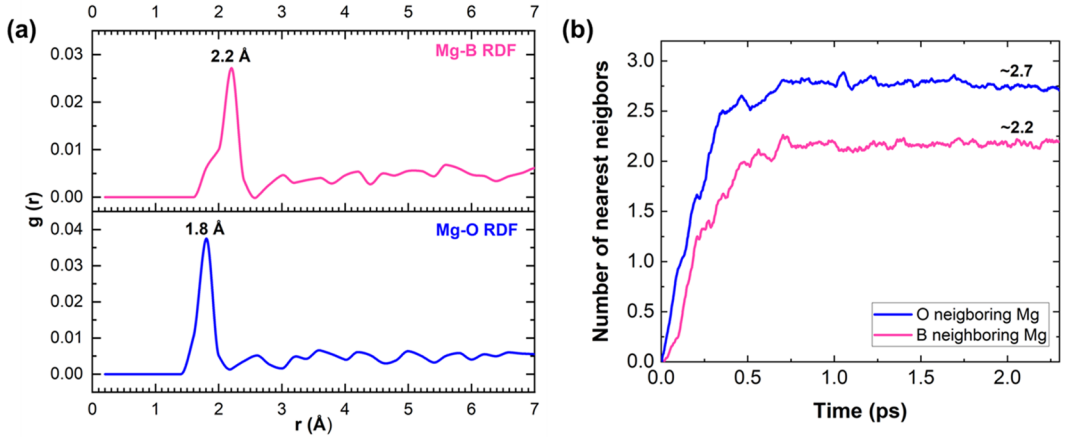

Figure 3. (a) Radial distribution function of pairwise Mg−O and Mg−B distances showing that the average Mg−O bond length is 1.8 Å and the average Mg−B bond length is 2.2 Å. (b) Average numbers of B and O occupying the nearest-neighbor sites of Mg are ∼2.2 and ∼2.7, respectively, indicating the formation of the $MgB_{2.2}O_{2.7}$ phase.

centers, and the density drops to zero at larger distances from the nuclei. Assuming a small perturbation in the charge density $n(r) = n(r) + \delta n$, Taylor expansion of the charge density-dependent Kohn−Sham total energy functional yields an energy expression which can be broadly divided into three terms as represented by eq 1:

$$E_{total} = E_{band\ structure} + E_{Coulombic} + E_{Repulsive} \quad (1)$$

$E_{band\ structure}$ represents all of the occupied electronic states and is evaluated from the DFTB Hamiltonian. $E_{Coulombic}$ contains the second-order and third-order long-range charge density fluctuation terms and is self-consistently evaluated from precomputed Hubbard U values of each atom. $E_{Repulsive}$ containing the ion−ion repulsion and the exchange correlation functional terms represents the bonded interactions in the first coordination sphere. Parameters of the $E_{Repulsive}$ part consisting of pairwise and three-body interactions were fitted by using the CHIMES training set. The CHIMES training set is developed by repulsive free computations of the DFTB forces and stress tensor components, which are subtracted from the DFT values of the same. The sums of the squares of the differences in the values of force and stress components calculated from DFT and repulsion free DFTB, respectively, are used to develop an objective function, from which the parameters for $E_{Repulsive}$ are obtained. A linear combination of Chebyshev polynomials accounts for pairwise and three-body interactions and is fed to the objective function as an input module to obtain the $E_{Repulsive}$ parameters.

The molecular dynamics simulations were performed in an NVT ensemble using a Nosé−Hoover thermostat.[40] We used a B_2O_3 − (001) surface (17.7 × 15.3 $Å^2$) created with total of 320 (B + O) atoms using the coordinates reported by a previous study[41] and optimized at 0 K. Periodic boundary conditions are applied to the simulation box, and the box length in the z direction 3 times larger than the thickness of the simulated surface to avoid wall effects on the vapor-phase atoms. The optimized surface is annealed at 2000 K to obtain a minimum-energy state via an NVT simulation. The Mg atoms were introduced as Mg vapor in the empty space above the equilibrated surface in the z direction. The magnitudes of the initial velocities are assigned from the Maxwell−Boltzmann distribution based on the ensemble temperature, whereas the direction of the velocities is assigned randomly. The MD simulation was performed with a time step of ∼0.1 fs and run over ∼3 ps to allow the Mg to be adsorbed on the B_2O_3 surface. The self-consistent charge DFTB calculation is performed to obtain the charge densities of the microstates formed at every MD step. The entire simulation has been performed using the DFTB+ package.[42] The obtained trajectory data have been using in-house scripts, and visual molecular dynamics (VMD) has been used to create visual representations of the surface from the trajectory data. All of the time-resolved data presented have been moving averaged over ∼100 MD steps.

RESULTS AND DISCUSSION

Surface Optimization, Equilibration, and Mg Introduction. The B_2O_3 (001) surface optimized at 0 K (Figure 2(a)) was equilibrated at the simulation temperature (2000 K) by running an MD simulation in an NVT ensemble. After the energy minimization (Figure S1, Supporting Information), one of the equal energy microstates (∼1.1 ps) is chosen as the relaxed surface, free Mg atoms are introduced above the surface (Figure 2(c)), and initial velocities are assigned from the Maxwell−Boltzmann distribution based on the simulation temperature. The snapshot of the relaxed surface (Figure 2(a)) shows considerable restructuring significantly altering the ordering and distances between the B and the O atoms. It is evident from the visual representations that there is no long-range order in the relaxed surface. The radial distribution function (Figure 2(b)) of pairwise distances between B and O at 0 K consists of two strong peaks at 1.3 and 3 Å, corresponding to the B−O bond distance and the distance of the B from the O attached to the neighboring B, respectively (Figure 2(a)). No other peaks exist between 1.4 and 2.9 Å, indicating the presence of long-range order in the system as evident from the visual snapshots. Multiple peaks emerge between 1.3 and 3 Å in the pair-correlation function of the B_2O_3 surface equilibrated to 2000 K indicating the absence of any long-range order. The absence of long-range ordering in the surface equilibrated to 2000 K makes it an ideal replica of the realistic B_2O_3 shell under reaction conditions, which exists in an amorphous state at room temperature and melts at ∼720 K.[1,43]

The simulations with the Mg were run for ∼3 ps, which was sufficient to study the bond breakage and formation on Mg

https://doi.org/10.1021/acs.langmuir.3c00982
Langmuir 2023, 39, 13782−13789

attachment to the surface. Figure 2(c) shows the representative snapshot of a microstate formed by the surface with adsorbed Mg at picoseconds time scales. The analysis for one particular Mg from the particular microstate shows that the Mg−O bond length is 1.9 Å, and the Mg−B bond distance is 2.2 Å. A representative video of the simulation trajectory has been included as SV1. Figure S2 contains the visual representation of the optimized surface, equilibrated surface, and surface with adsorbed Mg from different angles. For better statistical interpretation, an analysis over all of the microstates and the surroundings of all of the adsorbed Mg has been analyzed and presented in the rest of the article.

Mg Oxidation and Formation of the Mg−B−O Phase. The radial distribution functions representing the pairwise distances between Mg−O and Mg−B (Figure 3(a)) show that the mode of the Mg−O bond distance is 1.8 Å, whereas it is 2.2 Å for Mg−B. This suggests that the Mg prefers proximity to the O sites over that of the B sites, as expected from electronegativity differences. Figure 3(b) shows the time evolution of the occupancy of the nearest-neighboring sites of Mg by B and O. The average coordination of O (∼2.7) surrounding Mg is higher than the average of B (∼2.2) surrounding the Mg, which also indicates that Mg atoms prefer to be in the vicinity of O over that of B. The nearest-neighbor distribution also suggests that Mg tends to form the $MgB_{2.2}O_{2.7}$ phase after reaction with the B_2O_3 surface.

Figure 4 shows the temporal evolution of the average z-height and the relative change in the oxidation state of Mg which eventually becomes adsorbed on the B_2O_3 surface. The Mg moves to positions with lower z coordinates as they approach the surface from the vapor phase, and the value of the z coordinate becomes constant, indicating their adsorption on the B_2O_3 surface. The average oxidation state of the adsorbed Mg atoms simultaneously increases by +1, which signifies that the Mg atoms have been oxidized on the B_2O_3 surface. According to the Mg−B−O phase diagram,[44] different mixed-oxide phases such as MgB_4O_7, $Mg_2B_2O_5$, and $Mg_3B_2O_6$ can form on reaction of Mg with B_2O_3. In all of these oxide phases, Mg is bonded to O with an average bond distance of ∼1.7−1.9 Å. Thus, Figures 3 and 4 confirm that the adsorbed Mg is indeed oxidized on B_2O_3, with the average bond length being ∼1.8 Å. Mg-lean systems, upon complete reaction, should form a MgB_4O_7 phase. Since the simulated system is Mg-lean, it tends to form $MgB_{2.2}O_{2.7}$, which can potentially evolve into MgB_4O_7 on reaction completion at longer time scales.

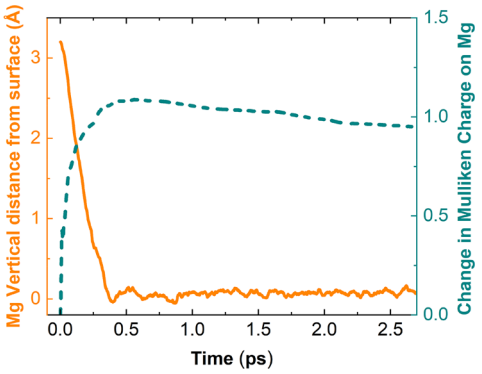

Figure 4. Decrease in the average z-height and increase in the Mulliken charge on adsorbed Mg, indicating the oxidation of the adsorbed Mg atoms on the B_2O_3 surface.

Rearrangement of B and O in the MgB_xO_y Phase. To understand the rearrangement of the atoms of O and B surrounding Mg during Mg−O bond formation, the displacement of the atoms of B and O with respect to Mg is temporally tracked. Figure 5 shows the displacement, $\Delta r = r(t) - r(0)$, of either B or O with respect to Mg as a function of time. Figure 5(a) shows a schematic representing the physical meaning of Δr. A positive Δr indicates a displacement away from Mg whereas a negative Δr indicates a displacement toward Mg. Figure 5(b) shows that on average the B are displaced away from Mg, whereas there is a net displacement of the O toward Mg by approximately the same extent. Thus, Mg displaces B from its previously occupied sites and attracts the O atoms to form the Mg−O bond in the Mg−B−O mixed oxide phase. The magnitude of the displacement of the neighboring O and B atoms toward or away from Mg is comparable to the ensemble-averaged displacement of all atoms (Figure S3), indicating that there is a significant extent of directional displacement of O and B atoms toward or away from Mg.

Bond Strain and Reduction of B at the MgB_xO_y−B_2O_3 Interface. It is essential to analyze the evolution of the oxidation state and the distance of the B initially bonded with the O that formed the Mg−O bond to understand the migration of atoms across the MgB_xO_y−B_2O_3 interface. Figure 6 shows that the aforementioned average O−B bond distance increases from ∼1.4 to 2 Å, resulting in an ∼40% bond strain, whereas the oxidation state of the corresponding B decreases

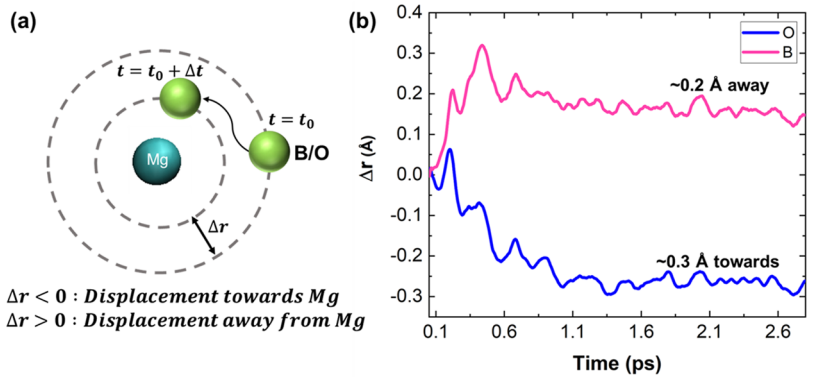

Figure 5. (a) Schematic explaining the significance of the evolution of Δr as a parameter to understand the directional displacement of B and O atoms toward or away from Mg. (b) Time evolution of Δr of B and O surrounding Mg shows that the B atoms are displaced away from Mg whereas the O atoms move toward Mg.

https://doi.org/10.1021/acs.langmuir.3c00982
Langmuir 2023, 39, 13782−13789

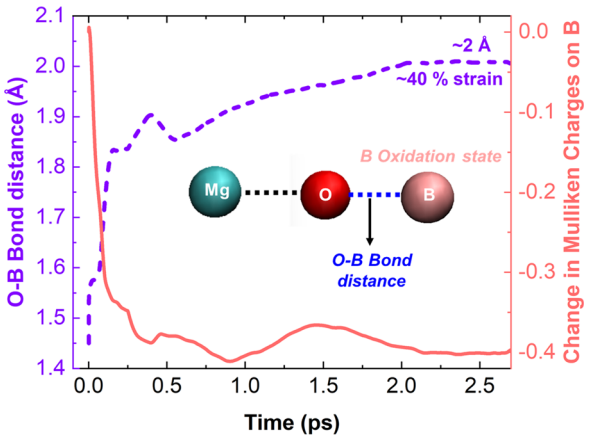

Figure 6. Time evolution of the O−B bond length at the MgB_xO_y−B_2O_3 interface, where the O is bonded to Mg, and the relative change in Mulliken charge on the respective B, showing that the length of the O−B bond extends with time and the attached B is reduced.

by 0.4. Figure S4 shows the oxidation states of B, Mg, and O with increasing z coordinate, at the initial state, and after ∼3 ps, which clearly shows that the oxidation state of B near the surface where Mg is adsorbed decreases by ∼0.4, implying that boron is getting reduced at the surface. Hence, the interfacial B atoms are undercoordinated and exist as immobilized free radicals (i.e., dangling bonds) ready to participate in surface reactions.[45]

The tensile strain in the evolving O−B bond should result in an excess volume of ∼20 Å^3. The excess volume can be accommodated either by the formation of regions of compressive strain in other locations of the lattice or by the expansion of the entire surface.[46] In this case, we observe that the minimum B−O bond distance is ∼1.3 Å, which is the equilibrium B−O bond distance,[47] and hence the possibility of the existence of compressive strains can be eliminated. Since the simulated surface is periodic in the x and y directions, a surface expansion can be registered only in the z direction. From Figure 7(a) it is evident that the surface expands in the z direction by ∼0.4 Å, which is approximately the same as that of the extension of the O−B bond length (∼0.6 Å). Thus, the excess volume created by tensile straining of the interfacial O−B bond is accommodated by the overall surface expansion, which implies that there is an overall tensile strain on the B_2O_3 surface. The expansion of the interstitial voids due to the overall tensile strain on the surface should imply an increase in the diffusivity of adsorbed species through the surface.

Effect on the Oxidation Rate of B Particles. To summarize, Mg adsorption on the B_2O_3 surface results in the formation of Mg-lean MgB_xO_y phases, which causes a rearrangement of the B and O atoms surrounding the adsorbed Mg. The oxygen exchange reaction leading to the Mg−O bond strains the remnant B−O bond, leading to a simultaneous reduction of the oxidation state of B (i.e., dangling bond formation). The O−B bond distance increase results in a tensile strain, and the excess volume created is accommodated by a net expansion of the surface. The B atoms with dangling bonds are active sites for gas-phase species adsorption. The net tensile strain on the surface should enhance the diffusivity of species from the surface to the bulk as explained by the schematic in Figure 8(a).

According to the Langmuir adsorption model,[48] the rate of adsorption of gases on a surface depends on the fraction of surface coverage as $r_{ads} = k_{ads}P(1 - \theta)$, where k_{ads} is the adsorption rate constant, P is the partial pressure of the gas-phase reactant, and θ is the fraction of surface coverage. For a fully oxidized B_2O_3 surface, θ should ideally be 1, and hence the rate of adsorption of gas-phase O_2 should be null. However, a B_2O_3 surface cannot practically exist as a pure B_2O_3 phase, as surface reconstruction (Figure 2(a)) always leads to uncoordinated atoms. For the sake of practical clarity, let us assume that a B_2O_3 surface has 99% O coverage. Consider a case with 10% (by number) adsorbed Mg. Given that the Mg forms an MgB_4O_7 phase on complete reaction, each Mg should pull one O out of the B_2O_3 phase, resulting in an ∼18.5% reduction in the number of O atoms in the B_2O_3 phase. This will create dangling bonds for ∼19.4% of B, thereby reducing θ to 0.81. In principle, this could provide an enhancement of ∼19× in the O_2 adsorption rate. (Figure 8(b)). It is well known that the interstitial diffusional flux (J) of a particular species scales linearly with the product of the diffusivity (D) and the interstitial volume increment relative to the volume of the diffusing atom (v_0, $J \approx Dv_0$), given that the gradient in strain remains constant.[46] Neglecting the fact that D is also influenced by the lattice strain to avoid complication, a bond length extension from 1.3 to 2.0 Å resulting in an ∼20 Å^3 volume increment should increase the flux of O atoms (radius ∼152 pm[49]) by 4×. Apart from the intrinsic reaction kinetics, the rate of oxidation of solid particles in gas-phase oxygen depends on (i) the rate of adsorption of gas-phase

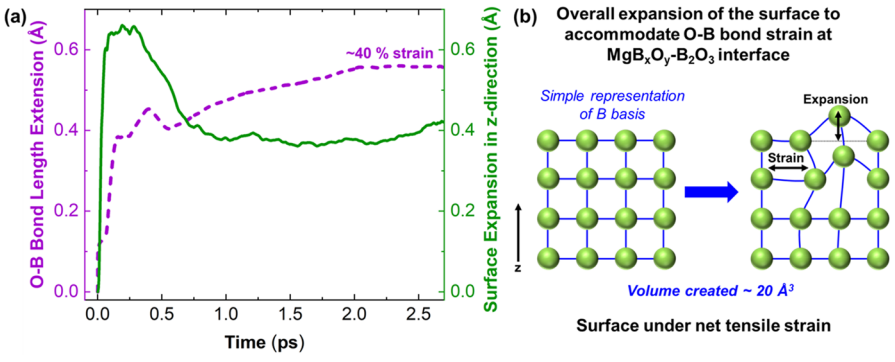

Figure 7. (a) Time evolution of the O−B bond length extension at the MgB_xO_y−B_2O_3 interface, where the O is bonded to Mg and the linear expansion of the surface is in the z direction. (b) Schematic explaining how the surface expands to accommodate the excess volume created by the extension in the O−B bond length, which results in an overall tensile strain.

https://doi.org/10.1021/acs.langmuir.3c00982
Langmuir 2023, 39, 13782−13789

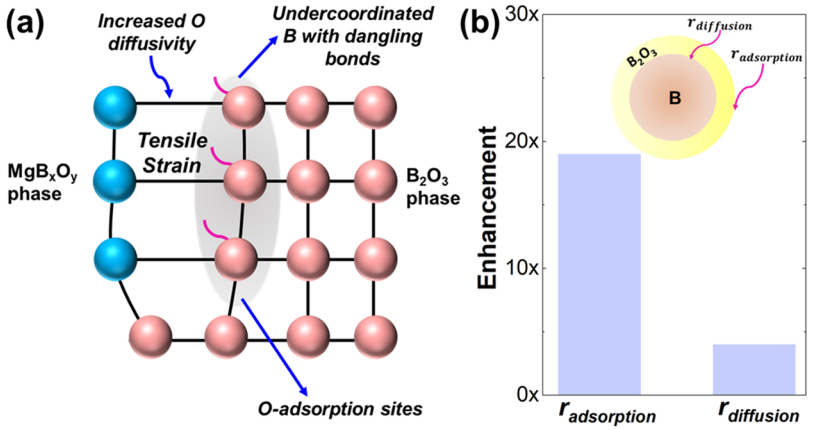

Figure 8. (a) Schematic showing the undercoordinated B existing at the MgB_xO_y–B_2O_3 interface possess dangling bonds which can act as active centers for O_2 adsorption as well as the straining of the interfacial B–O bond which will result in enhanced diffusion flux of adsorbed O. (b) Estimated enhancements in the rate of adsorption and diffusion of O to the B-particle interior based on simple continuum adsorption and diffusion models.

oxygen to the particle surface and (ii) the rate of diffusion of the adsorbed oxygen through the oxide shell to the particle interior.[50] Hence, for a B particle with a B_2O_3 shell, exposure to Mg vapor will result in the creation of immobilized B radicals at the surface of the oxide shell which will act as active centers for gas-phase O_2 adsorption, thereby increasing the rate of O_2 adsorption. Additionally, the Mg incorporation also results in a net tensile strain on the B_2O_3 surface, leading to an enhancement in the diffusivity of adsorbed O through the oxide shell. The combination of these two factors will simultaneously increase the rate of oxidation of the B particles.

CONCLUSIONS

We have computationally explored the reaction of vapor-phase Mg with the B_2O_3 surface using DFTB-MD simulations based on the CHIMES framework. We found that Mg becomes oxidized on the B_2O_3 surface to form the $MgB_{2.2}O_{2.7}$ phase, with the Mg–O bond length being 1.8 Å, which can potentially evolve into stoichiometric MgB_4O_7 phase on complete reaction. During the formation of the MgB_xO_y phase, there is a net displacement of B atoms away from Mg and O atoms toward Mg. As the Mg atoms pull the O atoms from B across the MgB_xO_y–B_2O_3 interface, a tensile strain develops in the B–O bond and the bond length is extended by ∼0.6 Å. We found that the surface expands along the z direction by ∼0.4 Å to accommodate the excess volume created by the straining of the interfacial bond, indicating the development of a net tensile strain. Simultaneously, B atoms at the interface are reduced to immobilized free radicals with dangling bonds that can act as active centers for gaseous O_2 adsorption, leading to an enhancement in the molecular oxygen adsorption rate on the surface. The tensile strain on the surface will increase the diffusion flux of adsorbed O atoms through the surface. As the rate of B-particle oxidation depends on both the oxygen adsorption rate and oxygen diffusion flux through the boron oxide shell, the enhancement of both of these rates will increase the overall oxidation rate of B particles. Hence, our findings provide sufficient mechanistic understanding of the enhancement in the oxidative energy release rates from B in the presence of Mg, as observed in previous experimental studies.

ASSOCIATED CONTENT

Supporting Information

The Supporting Information is available free of charge at https://pubs.acs.org/doi/10.1021/acs.langmuir.3c00982.

Surface energy, mean square displacements, and visual representation of the surface from different angles (PDF)

Simulation trajectory (MP4)

AUTHOR INFORMATION

Corresponding Author

Michael R. Zachariah – *University of California, Riverside, California 92521, United States;* orcid.org/0000-0002-4115-3324; Email: mrz@engr.ucr.edu

Authors

Prithwish Biswas – *University of California, Riverside, California 92521, United States;* orcid.org/0000-0002-9921-2905

C. Huy Pham – *Lawrence Livermore National Laboratory, Livermore, California 94550, United States*

Complete contact information is available at: https://pubs.acs.org/10.1021/acs.langmuir.3c00982

Notes

The authors declare no competing financial interest.

ACKNOWLEDGMENTS

This work has been supported by DTRA-funded MSEE URA and the ONR and was performed under the auspices of the U.S. Department of Energy by Lawrence Livermore National Laboratory under contract no. DE-AC52-07NA27344. We gratefully acknowledge Puja Agarwala at Penn State for compiling the Supporting Information video on the trajectory.

REFERENCES

(1) Wang, Y.; Wang, H.; Xu, F.; Ghildiyal, P.; Zachariah, M. R. Effect of Alkali Metal Perchlorate and Iodate Type on Boron Ignition: The Role of Oxidizer Phase Change. *Chem. Eng. J.* **2022**, *446*, 136786.

(2) Mursalat, M.; Schoenitz, M.; Dreizin, E. L. Effect of Particle Morphology on Reactivity, Ignition and Combustion of Boron Powders. *Fuel* **2022**, *324*, 124538.

(3) Veith, J.; Pfitzner, M. Combustion of Boron Particles in Premixed Methane/Air Flames. *Propell. Explos. Pyrot.* **2016**, *41*, 260−266.
(4) Chintersingh, K. L.; Schoenitz, M.; Dreizin, E. L. Boron Doped with Iron: Preparation and Combustion in Air. *Combust. Flame* **2019**, *200*, 286−295.
(5) Gottfried, J. L.; Wainwright, E. R.; Huang, S.; Jiang, Y.; Zheng, X. Probing Boron Thermite Energy Release at Rapid Heating Rates. *Combust. Flame* **2021**, *231*, 111491.
(6) Chintersingh, K. L.; Schoenitz, M.; Dreizin, E. L. Oxidation Kinetics and Combustion of Boron Particles with Modified Surface. *Combust. Flame* **2016**, *173*, 288−295.
(7) Baek, J.; Jiang, Y.; Demko, A. R.; Jimenez-Thomas, A. R.; Vallez, L.; Ka, D.; Xia, Y.; Zheng, X. Effect of Fluoroalkylsilane Surface Functionalization on Boron Combustion. *ACS Appl. Mater. Interfaces* **2022**, *14*, 20190−20196.
(8) Huang, S.; Deng, S.; Jiang, Y.; Zheng, X. Experimental Effective Metal Oxides to Enhance Boron Combustion. *Combust. Flame* **2019**, *205*, 278−285.
(9) Jiang, Y.; Dincer Yilmaz, N. E.; Barker, K. P.; Baek, J.; Xia, Y.; Zheng, X. Enhancing Mechanical and Combustion Performance of Boron/Polymer Composites via Boron Particle Functionalization. *ACS Appl. Mater. Interfaces* **2021**, *13*, 28908−28915.
(10) Chintersingh, K. L.; Schoenitz, M.; Dreizin, E. L. Transition Metal Catalysts for Boron Combustion. *Combust. Sci. Technol.* **2021**, *193*, 1400−1424.
(11) Young, G.; Sullivan, K.; Zachariah, M. R.; Yu, K. Combustion Characteristics of Boron Nanoparticles. *Combust. Flame* **2009**, *156*, 322−333.
(12) Zhao, W.; Wang, X.; Wang, H.; Wu, T.; Kline, D. J.; Rehwoldt, M.; Ren, H.; Zachariah, M. R. Titanium Enhanced Ignition and Combustion of Al/I2O5Mesoparticle Composites. *Combust. Flame* **2020**, *212*, 245−251.
(13) Zhao, W.; Wang, H.; Kline, D. J.; Wang, X.; Wu, T.; Xu, J.; Ren, H.; Zachariah, M. R. Influence of Titanium Addition on Performance of Boron-Based Thermites. *Chem. Eng. J.* **2022**, *438*, 134837.
(14) Yeh, C. L.; Kuo, K. K. Ignition and Combustion of Boron Particles. *Prog. Energy Combust. Sci.* **1996**, *22*, 511−541.
(15) Henz, B. J.; Hawa, T.; Zachariah, M. R. On the Role of Built-in Electric Fields on the Ignition of Oxide Coated Nanoaluminum: Ion Mobility versus Fickian Diffusion. *J. Appl. Phys.* **2010**, *107*, 024901.
(16) Trunov, M. A.; Umbrajkar, S. M.; Schoenitz, M.; Mang, J. T.; Dreizin, E. L. Oxidation and Melting of Aluminum Nanopowders. *J. Phys. Chem. B* **2006**, *110*, 13094−13099.
(17) Firmansyah, D. A.; Sullivan, K.; Lee, K. S.; Kim, Y. H.; Zahaf, R.; Zachariah, M. R.; Lee, D. Microstructural Behavior of the Alumina Shell and Aluminum Core before and after Melting of Aluminum Nanoparticles. *J. Phys. Chem. C* **2012**, *116*, 404−411.
(18) Huang, S.; Hong, S.; Su, Y.; Jiang, Y.; Fukushima, S.; Gill, T. M.; Yilmaz, N. E. D.; Tiwari, S.; Nomura, K. ichi; Kalia, R. K.; Nakano, A.; Shimojo, F.; Vashishta, P.; Chen, M.; Zheng, X. Enhancing Combustion Performance of Nano-Al/PVDF Composites with β-PVDF. *Combust. Flame* **2020**, *219*, 467−477.
(19) Nie, H.; Schoenitz, M.; Dreizin, E. L. Oxidation of Magnesium: Implication for Aging and Ignition. *J. Phys. Chem. C* **2016**, *120*, 974−983.
(20) Ghildiyal, P.; Biswas, P.; Herrera, S.; Xu, F.; Alibay, Z.; Wang, Y.; Wang, H.; Abbaschian, R.; Zachariah, M. R. Vaporization-Controlled Energy Release Mechanisms Underlying the Exceptional Reactivity of Magnesium Nanoparticles. *ACS Appl. Mater. Interfaces* **2022**, *14*, 17164−17174.
(21) Wagner, B.; Ghildiyal, P.; Biswas, P.; Chowdhury, M.; Zachariah, M. R.; Mangolini, L.; Wagner, B.; Mangolini, L.; Ghildiyal, P.; Biswas, P.; Chowdhury, M.; Zachariah, M. R. In-Flight Synthesis of Core-Shell Mg/Si-SiOx Particles with Greatly Reduced Ignition Temperature. *Adv. Funct. Mater.* **2023**, *33*, 2212805.
(22) Bazyn, T.; Krier, H.; Glumac, N. Evidence for the Transition from the Diffusion-Limit in Aluminum Particle Combustion. *Proc. Combust. Inst.* **2007**, *31*, 2021−2028.
(23) Law, C. K. A Simplified Theoretical Model for the Vapor-Phase Combustion of Metal Particles. *Combust. Sci. Technol.* **1973**, *7*, 197−212.
(24) Mohan, S.; Trunov, M. A.; Dreizin, E. L. On Possibility of Vapor-Phase Combustion for Fine Aluminum Particles. *Combust. Flame* **2009**, *156*, 2213−2216.
(25) Biswas, P.; Ghildiyal, P.; Kwon, H.; Wang, H.; Alibay, Z.; Xu, F.; Wang, Y.; Wong, B. M.; Zachariah, M. R. Rerouting Pathways of Solid-State Ammonia Borane Energy Release. *J. Phys. Chem. C* **2022**, *126*, 48−57.
(26) Biswas, P.; Wang, Y.; Herrera, S.; Ghildiyal, P.; Zachariah, M. R. Catalytic Cleavage of the Dative Bond of Ammonia Borane by Polymeric Carbonyl Groups for Enhanced Energy Generation. *Chem. Mater.* **2023**, *35*, 954−963.
(27) Balart, M. J.; Patel, J. B.; Gao, F.; Fan, Z. Grain Refinement of Deoxidized Copper. *Metall. Mater. Trans. A* **2016**, *47*, 4988−5011.
(28) Sun, Y.; Ren, H.; Jiao, Q.; Schoenitz, M.; Dreizin, E. L. Oxidation, Ignition and Combustion Behaviors of Differently Prepared Boron-Magnesium Composites. *Combust. Flame* **2020**, *221*, 11−19.
(29) Agarwal, P. P. K.; Matsoukas, T. Nanoenergetic Materials: Enhanced Energy Release from Boron by Aluminum Nanoparticle Addition. *ACS Omega* **2022**, *7*, 26560−26565.
(30) Agarwal, P. P. K.; Matsoukas, T. Low-Temperature Cost-Effective Synthesis of MgB2for Energetic Applications. *ACS Appl. Energy Mater.* **2022**, *5*, 15310−15315.
(31) Agarwal, P. P. K.; Matsoukas, T. Synthesis and Oxidation Chemistry of Highly Energetic Boron/Aluminum/Magnesium Composites. *FirePhysChem.* **2023**, *3*, 173.
(32) Agarwal, P. P. K.; Jensen, D.; Chen, C. H.; Rioux, R. M.; Matsoukas, T. Surface-Functionalized Boron Nanoparticles with Reduced Oxide Content by Nonthermal Plasma Processing for Nanoenergetic Applications. *ACS Appl. Mater. Interfaces* **2021**, *13*, 6844−6853.
(33) Agarwal, P. P. K.; Jensen, D.; Chen, C.-H.; Rioux, R. M.; Matsoukas, T. Synthesis and Characterization of Magnesium/Boron Solid Solutions for Energetic Applications. *ACS Appl. Energy Mater.* **2022**, *5*, 6716−6723.
(34) Ghildiyal, P.; Xu, F.; Rojas, A.; Wang, Y.; Chowdhury, M.; Biswas, P.; Herrera, S.; Abbaschian, R.; Zachariah, M. R. Magnesium-Enhanced Reactivity of Boron Particles: Role of Mg/B2O3 Exothermic Surface Reactions. *Energy Fuels* **2023**, *37*, 3272−3279.
(35) Foulkes, W. M. C.; Haydock, R. Tight-Binding Models and Density-Functional Theory. *Phys. Rev. B* **1989**, *39*, 12520.
(36) Seifert, G. Tight-Binding Density Functional Theory: An Approximate Kohn-Sham DFT Scheme. *J. Phys. Chem. A* **2007**, *111*, 5609−5613.
(37) Spiegelman, F.; Tarrat, N.; Cuny, J.; Dontot, L.; Posenitskiy, E.; Martí, C.; Simon, A.; Rapacioli, M. Density-Functional Tight-Binding: Basic Concepts and Applications to Molecules and Clusters. *Adv. Phys. X* **2020**, *5*, 1710252.
(38) Goldman, N.; Kweon, K. E.; Sadigh, B.; Heo, T. W.; Lindsey, R. K.; Pham, C. H.; Fried, L. E.; Aradi, B.; Holliday, K.; Jeffries, J. R.; Wood, B. C. Semi-Automated Creation of Density Functional Tight Binding Models through Leveraging Chebyshev Polynomial-Based Force Fields. *J. Chem. Theory Comput.* **2021**, *17*, 4435−4448.
(39) Lindsey, R. K.; Fried, L. E.; Goldman, N. ChIMES: A Force Matched Potential with Explicit Three-Body Interactions for Molten Carbon. *J. Chem. Theory Comput.* **2017**, *13*, 6222−6229.
(40) Evans, D. J.; Holian, B. L. The Nose-Hoover Thermostat. *J. Chem. Phys.* **1985**, *83*, 4069.
(41) Assaf, N. W.; De La Pierre, M.; Altarawneh, M. K.; Radny, M. W.; Jiang, Z. T.; Dlugogorski, B. Z. Structure, Stability, and (Non)Reactivity of the Low-Index Surfaces of Crystalline B2O3-I. *J. Phys. Chem. C* **2017**, *121*, 11346−11352.
(42) Hourahine, B.; Aradi, B.; Blum, V.; Bonafé, F.; Buccheri, A.; Camacho, C.; Cevallos, C.; Deshaye, M. Y.; Dumitric, T.; Dominguez, A.; et al. DFTB+, a Software Package for Efficient Approximate

https://doi.org/10.1021/acs.langmuir.3c00982
Langmuir 2023, 39, 13782−13789

Density Functional Theory Based Atomistic Simulations. *J. Chem. Phys.* **2020**, *152*, 124101.
(43) Sdiri, N.; Elhouichet, H.; Elakermi, E.; Dhifallah, A.; Ferid, M. Structural Investigation of Amorphous Na2O-P2O5-B2O3 Correlated with Its Ionic Conductivity. *J. Non Cryst. Solids* **2015**, *409*, 34−42.
(44) MUTLUER, T.; TIMUCIN, M. Phase Equilibria in the System MgO-B2O3. *J. Am. Ceram. Soc.* **1975**, *58*, 196−197.
(45) Kuzuya, M.; Ishikawa, M.; Noguchi, A.; Ito, H.; Kamiya, K.; Kawaguchi, T. Nature of Dangling-Bond Sites in Native Plasma-Polymerized Films of Unsaturated Hydrocarbons, and Electron Paramagnetic Resonance Kinetics on Heat Treatment of the Films. *J. Mater. Chem.* **1991**, *1*, 387−391.
(46) Grönbeck, H.; Zhdanov, V. P. Effect of Lattice Strain on Hydrogen Diffusion in Pd: A Density Functional Theory Study. *Phys. Rev. B* **2011**, *84*, 052301.
(47) Albert, B.; Hillebrecht, H. Boron: Elementary Challenge for Experimenters and Theoreticians. *Angew. Chem., Int. Ed.* **2009**, *48*, 8640−8668.
(48) Myong, R. S. Gaseous Slip Models Based on the Langmuir Adsorption Isotherm. *Phys. Fluids* **2004**, *16*, 104−117.
(49) Rivera Rocabado, D. S.; Nanba, Y.; Koyama, M. Density Functional Theory and Machine Learning Description and Prediction of Oxygen Atom Chemisorption on Platinum Surfaces and Nanoparticles. *ACS Omega* **2021**, *6*, 17424−17432.
(50) Park, K.; Lee, D.; Rai, A.; Mukherjee, D.; Zachariah, M. R. Size-Resolved Kinetic Measurements of Aluminum Nanoparticle Oxidation with Single Particle Mass Spectrometry. *J. Phys. Chem. B* **2005**, *109*, 7290−7299.

https://doi.org/10.1021/acs.langmuir.3c00982
Langmuir 2023, 39, 13782−13789